JCTC Journal of Chemical Theory and Computation

QM/MM Models of the O_2-Evolving Complex of Photosystem II

Eduardo M. Sproviero, José A. Gascón, James P. McEvoy, Gary W. Brudvig, and Victor S. Batista*

Department of Chemistry, Yale University, P.O. Box 208107, New Haven, Connecticut 06520-8107

Received January 11, 2006

Abstract: This paper introduces structural models of the oxygen-evolving complex of photosystem II (PSII) in the dark-stable S_1 state, as well as in the reduced S_0 and oxidized S_2 states, with complete ligation of the metal−oxo cluster by amino acid residues, water, hydroxide, and chloride. The models are developed according to state-of-the-art quantum mechanics/molecular mechanics (QM/MM) hybrid methods, applied in conjunction with the X-ray crystal structure of PSII from the cyanobacterium *Thermosynechococcus elongatus*, recently reported at 3.5 Å resolution. Manganese and calcium ions are ligated consistently with standard coordination chemistry assumptions, supported by biochemical and spectroscopic data. Furthermore, the calcium-bound chloride ligand is found to be bound in a position consistent with pulsed electron paramagnetic resonance data obtained from acetate-substituted PSII. The ligation of protein ligands includes monodentate coordination of D1-D342, CP43-E354, and D1-D170 to Mn(1), Mn(3), and Mn(4), respectively; η^2 coordination of D1-E333 to both Mn(3) and Mn(2); and ligation of D1-E189 and D1-H332 to Mn(2). The resulting QM/MM structural models are consistent with available mechanistic data and also are compatible with X-ray diffraction models and extended X-ray absorption fine structure measurements of PSII. It is, therefore, conjectured that the proposed QM/MM models are particularly relevant to the development and validation of catalytic water-oxidation intermediates.

1. Introduction

The photosynthetic water-oxidation reaction in the thylakoid membranes of cyanobacteria and green-plant chloroplasts releases $O_2(g)$ into the atmosphere according to the four-electron water-splitting reaction

$$2H_2O(l) \rightarrow O_2(g) + 4H^+ + 4e^- \quad (1)$$

The water-oxidation reaction, given by eq 1, is catalyzed by the so-called oxygen-evolving-complex (OEC) of photosystem II (PSII). This paper develops chemically sensible models of the OEC of PSII in which the Mn_3CaO_4Mn cluster is completely ligated by amino acid residues, water, hydroxide, and chloride ions. State-of-the-art quantum mechanics/molecular mechanics (QM/MM) hybrid methods[1−3] are applied in conjunction with the X-ray crystal structure of PSII from the cyanobacterium *Thermosynechococcus elongatus*,[4] explicitly addressing the perturbational influence of the surrounding protein environment on the structural and electronic properties of the OEC. The resulting structural models are analyzed by comparison to a large body of experimental data and mechanistic hypotheses of photosynthetic oxygen evolution.[5]

In contrast to chemical and electrochemical water oxidation reactions, which are thermodynamically highly demanding, the OEC-catalyzed water-splitting mechanism proceeds with very little driving force and requires only moderate activation energies.[6−9] Moreover, PSII turns over very rapidly, producing up to 50 dioxygen molecules per second. The high efficiency of the reaction has motivated extensive spectro-

* Corresponding author fax: (203) 432-6144; e-mail: victor.batista@yale.edu.

10.1021/ct060018l CCC: $33.50
Published on Web 05/02/2006

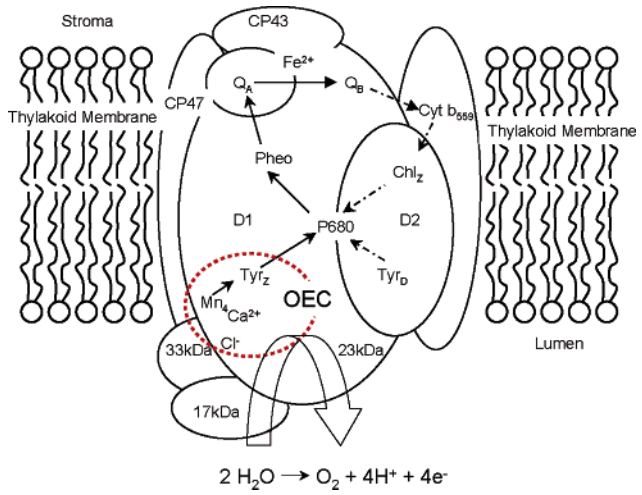

Figure 1. PSII complex and its antenna system, consisting of more than 20 protein subunits, either embedded in the thylakoid membrane or associated with its lumenal surface. Light energy is trapped predominantly by the outer antenna and transferred to the photochemically active reaction center, via light-harvesting proteins CP47 and CP43, where it is used to drive the water-splitting reaction at the OEC. The electrons extracted from water are passed from the lumenally located Ca/Mn cluster to $P680^+$ via D1-Y161 (Tyr_Z or Y_Z), a process that is coupled to ET from P680 to pheophytin (Pheo), to quinone electron acceptor Q_A, and onto quinone electron acceptor Q_B, near a nonheme iron group, defining the ET pathway marked by the solid arrows. Broken arrows indicate secondary ET pathways, which may play a photoprotective role. The protons and molecular oxygen produced during the water-splitting reaction are released into the lumen.

scopic and biochemical studies of PSII.[5,6,10,11] However, the complexity of the system and the lack of a complete and unambiguous structure of the OEC have so far hindered the development of rigorous theoretical studies, limiting calculations to QM descriptions of inorganic complexes isolated from the influence of the actual protein environment (see ref 12 and references therein), or more complete OEC models built according to classical MM methods.[13,14] Therefore, the development of computational studies in which both the intrinsic properties of the cluster and the influence of the protein environment are explicitly considered has yet to be reported and is the subject of this paper.

A complete functional model of the OEC remains elusive, although extensive work over many years of study has provided considerable insight into the OEC functionality and the underlying catalytic mechanism of photosynthetic water oxidation. It is, nowadays, established that photoabsorption by the specialized chlorophyll *a* species, P680, triggers a chain of electron transfer (ET) reactions (see Figure 1). The excited singlet state of P680 decays to the oxidized state $P680^+$ by ET to a nearby pheophytin (Pheo) in about 2 ps after photoexcitation of P680. The charge-separated state is stabilized by a subsequent ET to a primary quinone electron acceptor (Q_A), which functions as a one-electron carrier, and subsequently to a secondary quinone electron acceptor (Q_B), which functions as a two-electron carrier, exchanging with free quinone upon two-electron reduction. The photo-

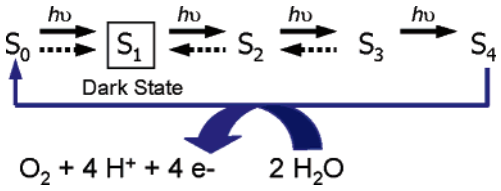

Figure 2. Kok cycle describing photosynthetic water oxidation by the reduction of the OEC from the S_4 to the S_0 state. Dotted arrows indicate reactions that relax the system back to the dark stable state S_1 within minutes. For simplicity, deprotonation reactions during the $S_0 \rightarrow S_1$, $S_2 \rightarrow S_3$, and $S_3 \rightarrow S_4$ oxidation steps are omitted.

oxidized chlorophyll *a* species $P680^+$ is reduced by a redox-active tyrosine (Y_Z), which is, in turn, reduced by the oxidation of water, catalyzed by the OEC.

The catalytic cycle of Joliot et al. and Kok et al.[15,16] (see Figure 2) constitutes the basis of our current understanding of photosynthetic water oxidation as well as the foundation for further studies on the chemical nature of the reaction intermediates. The Kok cycle includes five oxidation states of the OEC, which are called storage states or simply "S states". Each photoinduced ET from P680 to Q_A oxidizes the OEC to a higher S state. The most oxidized state (S_4) is quickly reduced to the S_0 state by the four-electron water-oxidation reaction, given in eq 1. In the dark, the S_0, S_2, and S_3 states are meta-stable and transform into the S_1 state within minutes (Figure 2, dashed lines). Hence, extensively dark-adapted samples contain only the S_1 state. Because this is the most easily characterized S state, it is our starting point for structural studies of the OEC of PSII. A number of structural models of the OEC[6−9,11,12,17,18] with mechanistic implications[5,13,14,18−23] have been proposed in attempts to rationalize the catalytic cycle at the detailed molecular level. However, many fundamental aspects of the proposed mechanisms and structure intermediates are the subject of current debate.[14,18,19] In fact, unequivocal functional models of the OEC S states are yet to be established.

Until recently, all structural information regarding the OEC and its local environment has been derived from a variety of spectroscopic and biochemical techniques,[11,24−27] including electron paramagnetic resonance (EPR) spectroscopy,[23,28−32] X-ray absorption spectroscopy (XAS),[33−38] optical spectroscopies,[39] Fourier transform infrared spectroscopy,[40−44] and site-directed mutagenesis.[45−48] In recent years, however, several groups have published X-ray diffraction structures of PSII from the cyanobacteria *Thermosynechococcus elongatus* and *Thermosynechococcus vulcanus*, yielding structures at 3.0−3.8 Å resolution.[4,49−52] In particular, the recently published X-ray crystal structure of cyanobacterial PSII (PDB access code 1S5L)[4] resolves most of the amino acid residues in the protein and nearly all cofactors at 3.5 Å resolution and suggests an atomic model of the OEC metal center (see Figure 3), providing a great opportunity for rigorous theoretical studies.

There are many aspects of the X-ray diffraction structure that have met with criticism, including both the geometric features of the Mn cluster[36,38] and the proposed ligation scheme.[13,14,19,42−44] In addition to the moderate resolution,

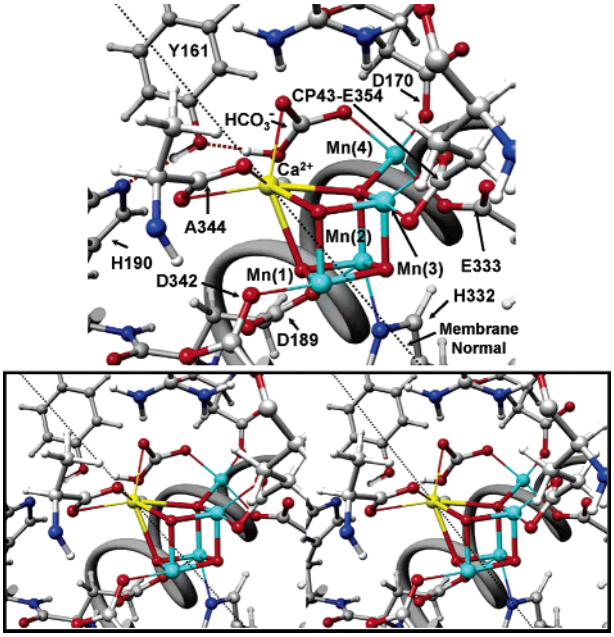

Figure 3. X-ray structure of the OEC of PSII.[4] Upper and lower panels show the OEC and surrounding residues in mono- and stereoviews, respectively. Note that all amino acid residues correspond to the D1 protein subunit, unless otherwise indicated.

the X-ray diffraction data might correspond to a photoreduced Mn cluster due to the high doses of X-rays employed.[4,53] Therefore, the proposed X-ray diffraction models of the OEC remain rather controversial.

In fact, to date, the precise positions of the individual Mn ions could not be resolved in any X-ray diffraction model because the coordinate error in the resulting density maps is usually as high as 1 Å[50] and the resolution of bridging ligands is typically out of reach.[36] Because of these limitations, the model of the OEC metal center in the 1S5L structure, including the "3 + 1 Mn tetramer" proposed by EPR spectroscopic studies,[23,35] has been based both on the overall electronic density maps and on the Mn−Mn distances reported by previous XAS studies.[20,54,55] The proposed Mn tetramer (see Figure 3) takes the form of a Mn_3CaO_4 cuboidal cluster, including three closely associated manganese ions linked to a single μ_4-oxo-ligated Mn ion, often called the "dangling manganese ion". The proposed cuboidal model is still the subject of current debate[36] and disagrees with previously proposed structures in which three Mn ions were placed roughly at three corners of an isosceles triangle, with the fourth Mn ion at the center of the triangle either protruding toward the lumenal surface of the membrane[49,50] or parallel to it.[52] The 1S5L crystallographic model also assigns potential protein ligands to the cluster (see Figure 3), including several amino acid residues already thought to be ligands on the basis of site-directed mutagenesis and spectroscopic studies.[47,48] However, the number of protein ligands is surprisingly small, especially considering that Mn ions in high-oxidation states are usually coordinated by five or six ligands. The X-ray structure makes up for part of the ligand deficit by suggesting the presence of a bicarbonate anion bridging Ca^{2+} and Mn(4). Furthermore, a number of small, nonprotein ligands, such as substrate and nonsubstrate water molecules, as well as hydroxide and chloride ions, are not visible at the current resolution.

Considering that QM/MM studies have played an essential role in revealing structure−function relations in a variety of other biological systems,[3,56−71] it is expected that many of the controversial aspects of PSII could be resolved by combining the analysis and interpretation of experiments with rigorous QM/MM studies. Despite the incomplete and somewhat provisional nature of the 1S5L crystallographic structure, the proposed cluster architecture constitutes the most valuable point of departure for developing complete functional models of the OEC. The structural models developed in this paper, therefore, build upon the 1S5L structure. Density functional theory (DFT) QM/MM hybrid methods are applied to obtain completely ligated model structures of the OEC in the S_1 state, in an effort to determine whether the proposed 1S5L architecture can lead to a chemically sensible molecular structure of the hydrated OEC in the S_1 state with a complete coordination by water, protein ligands, hydroxide, and Cl^- ions. The resulting QM/MM structural models are analyzed in terms of the intrinsic structure of the proposed Mn_3CaO_4Mn unit, embedded in the protein environment, as compared to structural XAS data. Some of the important questions addressed by the structural analysis are as follows: How many Mn−Mn vectors of ∼2.7 Å are predicted by QM/MM models in the S_1 state? What is the most likely binding site for chloride? What proteinaceous ligating motifs give rise to the observed Mn−Mn distances? Finally, considering that water is the substrate for the catalytic reaction and that the positions of water molecules are unlikely to be resolved even by considerably higher-resolution X-ray structures, what are the implied locations of water molecules? Are those compatible with catalysis? The analysis of these fundamental aspects suggests that QM/MM hybrid methods, applied in conjunction with the X-ray crystallographic data, can considerably extend the description of the OEC into chemically sensible models with complete coordination of the metal cluster.

The paper is organized as follows. Section 2 describes the methodology, including the preparation of QM/MM structural models, the description of the QM/MM methodology, and the theoretical methods applied for simulations of extended X-ray absorption fine structure (EXAFS) spectra. Section 3 presents the results and a discussion with emphasis on mechanistic implications. Section 4 summarizes and concludes.

2. Methodology

2.1. Molecular Models. Molecular models are based on the 1S5L X-ray crystal structure of PSII (see Figure 3).[4] The models build upon previous work,[13,14] explicitly considering 1987 atoms of PSII, including the proposed Mn_3CaO_4Mn unit and all amino acid residues with α-carbons within 15 Å from any atom in the OEC metal ion cluster, with the addition of a buffer shell of amino acid residues with α-carbons within 15−20 Å from any atom in the OEC ion cluster. The coordination of the Mn ions was completed by

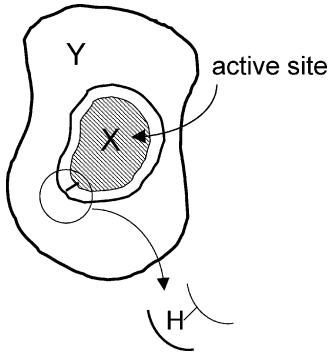

Figure 4. Partition of the biomacromolecular system into a reduced system (region X) and the surrounding molecular environment (region Y).

hydration, assuming a minimum displacement of the ligating residues from their crystallographic positions and the usual coordination of five or six ligands to Mn ions with oxidation states III and IV, respectively. The variable coordination of calcium, typically with six to eight ligands, was satisfied by the coordination resulting from geometry optimization of the water molecules and negative counterions.

The 1S5L X-ray crystal structure of the OEC is consistent with several possible binding sites for water molecules,[4] including Ca^{2+} as suggested by ^{18}O isotope exchange measurements.[26,72] Hydrated models were constructed by "soaking" the molecular structures in a large box containing a thermal distribution of water molecules and keeping those water molecules that did not sterically interfere with the protein residues or with existing water molecules in the model.[14] The complete structures were subsequently relaxed. Because geometric optimization often creates new cavities, a series of soaking and relaxation procedures was applied until the number of water molecules converged. Such a computational protocol usually resulted in the addition of ~85 water molecules, with a few of them (up to six molecules) attached to calcium and manganese ions in the cuboidal Mn_3CaO_4Mn cluster. Two of the ligated waters bound to Ca^{2+} and Mn(4) are probable substrate water molecules, responsible for O−O bond formation in the $S_4 \rightarrow S_0$ transition. The resulting hydration of the cluster is, thus, roughly consistent with pulsed EPR experiments, which reveals the presence of several exchangeable deuterons near the Mn cluster in the S_0, S_1, and S_2 states.[23]

2.2. QM/MM Hybrid Approach. QM/MM computations are based on the two-layer ONIOM electronic-embedding (EE) link-hydrogen atom approach[2] as implemented in Gaussian 03.[73] The ONIOM QM/MM methodology could only be efficiently applied to studies of the OEC of PSII after obtaining high-quality initial-guess states for the ligated cluster of Mn ions (i.e., the reduced system) according to ligand field theory[74] as implemented in Jaguar 5.5.[75] The resulting combined approach allowed us to exploit important capabilities of ONIOM, including both the link-hydrogen atom scheme for efficient and flexible definitions of QM layers and the possibility of modeling open-shell systems by performing unrestricted DFT (e.g., UB3LYP) calculations.

The ONIOM-EE method is applied by partitioning the system, as described in Figure 4, according to a reduced molecular domain (region X) that includes the Mn_3CaO_4-Mn complex and the directly ligating proteinaceous carboxylate groups of D1-D189, CP43-E354, D1-A344, D1-E333, D1-D170, D1-D342, and the imidazole ring of D1-H332,[76] as well as bound water molecules, hydroxide, and chloride ions. The rest of the system defines region Y. The QM/MM boundaries are defined for the corresponding amino acid residues (i.e., D1-D189, CP43-E354, D1-A344, D1-E333, D1-D170, D1-D342, and D1-H332), by completing the covalency of frontier atoms according to the standard link-hydrogen atom scheme depicted in Figure 4.

The total energy E of the system is obtained at the ONIOM-EE level from three independent calculations as follows

$$E = E^{\mathrm{MM,X+Y}} + E^{\mathrm{QM,X}} - E^{\mathrm{MM,X}} \qquad (2)$$

where $E^{\mathrm{MM,X+Y}}$ is the energy of the complete system computed at the molecular-mechanics level of theory, while $E^{\mathrm{QM,X}}$ and $E^{\mathrm{MM,X}}$ correspond to the energy of the reduced system computed at the QM and MM levels of theory, respectively. Electrostatic interactions between layers X and Y are included in the calculation of both $E^{\mathrm{QM,red}}$ and $E^{\mathrm{MM,red}}$, at the quantum mechanical and molecular mechanical levels, respectively. Therefore, the electrostatic interactions computed at the MM level in $E^{\mathrm{MM,red}}$ and $E^{\mathrm{MM,full}}$ cancel. Thus, the resulting QM/MM evaluation of the total energy at the ONIOM-EE level includes a quantum mechanical description of polarization of the reduced system due to the electrostatic influence of the surrounding protein environment. The analogous QM/MM method where the polarization of the reduced system is neglected is called ONIOM molecular embedding (ME). The self-consistent polarization of the protein environment is modeled according to the "moving domain−QM/MM" (MoD-QM/MM) approach,[3] outlined in section 2.3.

The efficiency of the QM/MM calculations is optimized by using a combination of basis sets for the QM layer, including the lacvp basis set for Mn ions in order to consider nonrelativistic electron core potentials, the 6-31G(2df) basis set for bridging O^{2-} ions in order to include polarization functions on μ-oxo bridging oxides, and the 6-31G basis set for the rest of the atoms in the QM layer. Such a choice of basis set has been validated through extensive benchmark calculations on high-valent manganese complexes.[12,77] The molecular structure beyond the QM layer is described by the Amber MM force field. Fully relaxed QM/MM molecular structures are obtained at the ONIOM-EE (UHF B3LYP/lacvp,6-31G(2df),6-31G:AMBER) level of theory by geometry optimization of the complete structural models in the presence of a buffer shell of amino acid residues with α-carbons within 15−20 Å from any atom in the OEC ion cluster. These are subject to harmonic constraints in order to preserve the natural shape of the system.

The electronic states of the structural models, fully relaxed at the ONIOM QM/MM level of theory, involve antiferromagnetic couplings between manganese centers. These couplings define broken-symmetry states, providing multiconfigurational character to the singlet state S_1.[78−81] A typical optimization procedure involves the preparation of the QM

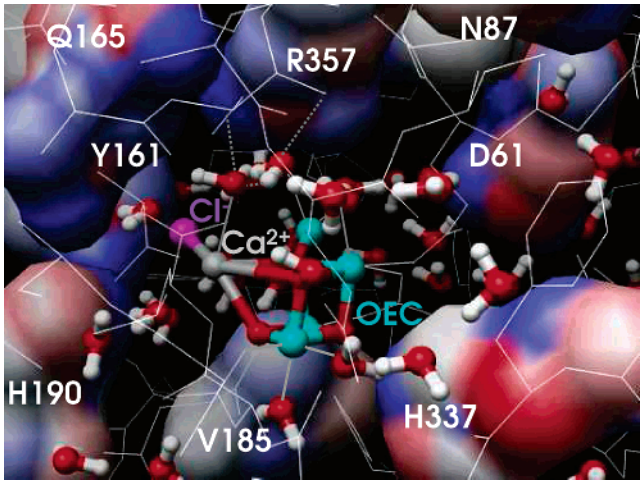

Figure 5. Quantitative analysis of the effect of protein polarization on the charge distribution of amino acid residues surrounding the Mn_3CaO_4Mn cuboidal cluster of the OEC. Blue (red) colors indicate an increase (decrease) in electronic density due to polarization effects (maximum differences, indicated by bright coloring, correspond to changes of atomic charges of about ±15−20%). Note that all amino acid residues correspond to the D1 protein subunit, unless otherwise indicated.

layer in various possible initial spin states, stabilized by specific arrangements of ligands. The subsequent geometry relaxation, carried out at the ONIOM DFT−QM/MM level of theory, locally minimizes the energy of the system by finding the optimized geometry and spin-electronic state. The purity of the state is preserved throughout the geometry optimization process, in the event that the initial-guess electronic state is compatible with the geometry of the Mn_3CaO_4Mn cluster and the specific arrangement of ligands, and there are no other spin states of similar energy found along the optimization process. Otherwise, the optimization process changes the electronic spin state to the ground electronic-state symmetry of the corresponding nuclear configuration. The resulting optimized structures are analyzed and evaluated not only on the basis of the total energy of the system but also as compared to structural, electronic, and mechanistic features that should be consistent with experimental data.

2.3. Polarization of the Protein Environment. Modeling the electrostatic interactions between the QM and MM layers of the OEC of PSII is a challenging task because the high-valent multinuclear oxomanganese cluster Mn_3CaO_4Mn is embedded in a polarizable protein environment, ligated by protein ligands, water, hydroxide, and chloride ions. To describe the resulting self-consistent polarization of the system, the ONIOM-EE method has been applied in conjunction with the MoD-QM/MM computational protocol.[3]

The protocol MoD-QM/MM involves a simple space domain decomposition scheme where electrostatic potential (ESP) atomic charges of the constituent molecular domains are computed, to account for mutual polarization effects, and iterated until obtaining a self-consistent point-charge model of the electrostatic potential. This is particularly relevant for systems where polarization effects make inappropriate the use of standard molecular mechanics force fields.

Figure 5 shows a color map of the OEC residues, displaying differences in atomic charges obtained by considering, or neglecting, the mutual electrostatic influence at the ONIOM-EE and ONIOM-ME levels of theory, respectively. The residues that are more significantly polarized by the oxomanganeses cluster are CP43-R357, D1-H337, D1-Q165, D1-Y161, D1-N87, D1-H190, D1-D61, and D1-V185, in addition to the residues directly ligated to Mn ions. Furthermore, it is shown that protein polarization, induced by the high-valent multinuclear oxomanganese cluster ions, usually introduces small corrections (∼7−20) to the values of atomic charges of surrounding amino acid residues. However, summing these corrections over the whole QM-MM interface typically corrects the total QM/MM energy by 10−15 kcal/mol. The overall energy correction is, thus, significant (e.g., comparable to the energy-level splitting between high-spin and low-spin states of the Mn tetramer) and, therefore, necessary for accurate descriptions of the structure of the OEC of PSII.

2.4. EXAFS Simulations. Simulations of EXAFS spectra of the proposed structural models allow one to make direct comparisons with experimental data. Simulations of EXAFS spectra consider that a monochromatic X-ray beam is directed at a sample and that the photon energy of the X-rays is gradually increased such that it traverses one of the absorption edges of the elements contained within the sample. When the energy is below the absorption edge, the photons cannot excite the electrons of the relevant atomic level, and thus, absorption is low. On the other hand, when the photon energy is sufficiently high, a deep core electron is excited into a state above the Fermi energy. The resulting increase in absorption is known as the absorption edge. The ejected photoelectrons usually have low kinetic energy and can be backscattered by the atoms surrounding the emitting atom source. The interference of these outgoing photoelectrons with the scattered waves from atoms surrounding the central atom causes EXAFS. The regions of constructive and destructive interference are seen as local maxima and minima giving rise to oscillations in EXAFS intensities. These oscillations can be used to determine the atomic number, the distance and coordination number of the atoms surrounding the element whose absorption edge is being examined, the nature of neighboring atoms (their approximate atomic number), and changes in central-atom coordination with changes in experimental conditions.

The theory of the oscillatory structure, due to scattering of the photoelectron (emitted upon absorption of the X-ray) by atoms surrounding the emitting atom, was originally proposed by Kronig[82,83] and worked out in detail by Sayers et al.,[84] Stern,[85] Lee and Pendry,[86,87] and Ashley and Doniach.[88] Here, we outline only briefly the calculation of a typical EXAFS experiment, where a monochromatic X-ray beam passes through a homogeneous sample of uniform thickness x.

The absorption coefficient $\mu(E)$ is related to the transmitted (I) and incident (I_0) fluxes by $I = I_0 \exp[-\mu(E)x]$. In the weak-field limit, it is assumed that the main contribution to XAS comes from a dipole-mediated transition. In particular, when an electron in a deep core state i is excited into an

unoccupied state *f*, the absorption probability is given by time-dependent perturbation theory and is proportional to the square of the transition matrix element:

$$\mu(E) \sim \sum_{f}^{E_f<E_F} |\langle f|\hat{\epsilon}\cdot\vec{r}\ \exp(i\vec{\kappa}\cdot\vec{r})|i\rangle^2 \delta(E_f) \quad (3)$$

where E_F is the Fermi energy and $\hat{\epsilon}$ and $\vec{\kappa}$ are the X-ray electric polarization and the wave vector, respectively. In the dipole approximation, the exponential is neglected and the absorption probability is independent of the direction of the sample axes with respect to $\hat{\epsilon}$.

There are two ways to solve eq 3. One method involves finding an adequate representation of the *i* and *f* states and then evaluating the integral directly. The other approach involves multiple scattering theory, where eq 3 can be written as follows:

$$\mu(E) \propto -\frac{1}{\pi} Im\langle i|\hat{\epsilon}^*\cdot\vec{r}\ G_{r,r'}(E)\ \hat{\epsilon}\cdot\vec{r}'|i\rangle\ \Theta(E-E_F) \quad (4)$$

with G and Θ representing the Green and Heaviside functions, respectively.

The results reported in this paper are based on the real space Green's function (RSGF) approach,[89] which has several advantages over traditional electronic-structure methods, especially for complex systems. The RSGF approach is essential for processes such as X-ray absorption, where symmetry-breaking effects (e.g., the photoelectron mean free path damping due to core-hole and inelastic losses) must be taken into account.

The central quantity in RSGF calculations is the matrix form of the propagator $G_{L'R',LR}(E)$ in a representation $|LR\rangle = i^l j_l(kr_R)Y_{lm}(\hat{r}_R)$, for site R and angular momentum $L = (l, m)$, where $\vec{r}_R = \vec{r} - \vec{R}$ and $L = (l, m)$. The matrix elements represent the transition amplitudes for an electron to propagate between states $|LR\rangle$ and $|L'R'\rangle$, satisfying the multiple-scattering equations[90] for a cluster with N_R sites,

$$G = G^C + G^{SC}$$
$$G^{SC} = e^{i\delta}\,[\mathbf{1} - G^0T]^{-1}G^0\,e^{i\delta'} \quad (5)$$

Here, the matrix indices are suppressed for simplicity, G^C represents the central atom contribution, G^{SC} is the scattering part from the surroundings, G^0 represents the damped free propagators, and T is the dimensionless scattering matrix which incorporates the spherical scattering potentials in terms of partial phase shifts for individual sites.

Once the propagator is obtained by solving eq 5, many physical quantities can be calculated. For example, the contribution to the X-ray absorption spectra from a given site and final state angular momentum L (with a relaxed core hole) is given by the golden rule expression

$$\mu(E) \sim -\frac{1}{\pi} Im\sum_{L,L'} M_{L'}^*(E)\ G_{L'0,L0}(E)\ M_L(E) \quad (6)$$

where $M_L(E) = \langle L, 0|\hat{\epsilon}\vec{r}|c\rangle$ is a transition dipole matrix element between the atomic core state and a local final state $|L, 0\rangle$, with $\hat{\epsilon}$ being the X-ray polarization vector.

The total absorption coefficient $\mu(E)$ can be conveniently described as the isolated atom absorption $\mu_0(E)$ times a correction factor: $\mu = \mu_0(1 + \chi)$, where χ is the fractional change in absorption coefficient induced by neighboring atoms. Within the context of the single scattering approximation, a simple expression for χ is known as 'the standard EXAFS equation' for K-edge excitation.[84] According to such an equation, the contribution to EXAFS of an atom (index *i*) is given by

$$\chi(k) = Im\sum_i \left(\frac{N_i S_0^{\,2}\, F_i(k)}{kR_i^{\,2}} \exp\{i[2\kappa R_i + \Phi_i(k)]\} \exp(-2\sigma_i^2 k^2) \exp[-2R_i/\lambda(k)] \right) \quad (7)$$

where k is the wave vector modulus for the photoelectron; N_i is the number of atoms of type i at distance R_i from the absorber; the Debye−Waller factor $\exp(-2\sigma_i^2k^2)$ takes account of fluctuations of distances due to a structural or thermal disorder, under the assumption of small displacements and Gaussian distributions of distances; the exponential term $\exp[-2R_i/\lambda(k)]$ takes account of finite elastic mean free paths of photoelectrons $\lambda(k)$ (between 5 and 10 Å for photoelectron energies from 30 to 1000 eV); S_0^2 is an average amplitude reduction factor (its value, usually 0.8−0.9, is the percent weight of the main excitation channel with respect to all possible excitation channels); $F_i(k)$ is a scattering amplitude function characteristic of the ith atom; $\Phi_i(k)$ is a phase function that takes account of the varying potential field along which the photoelectron moves. Equation 7 is valid in the case of nonoriented samples.

In this paper, the Fourier transform (FT) of $k^3\chi(k)$ is performed with a Kaiser−Bessel-type window. The FT amplitude is normalized so that the maximum amplitude of the simulated spectrum coincides with the maximum amplitude of the experimental spectrum. To model the total number of electrons, the Fermi energy is taken as a free parameter to fit the relative peaks of the simulated spectrum to the experiment. EXAFS simulations on benchmark model compounds, for which high-resolution X-ray structures are known, tend to overestimate the apparent distances by about 0.15 Å. Thus, this shift was also applied to the EXAFS calculations reported here. The QM/MM structural models of the OEC of PSII are analyzed and partially validated by performing simulations of EXAFS spectra, explicitly considering $N_R \sim 10^3$ atomic sites with s, p, and d electrons. Simulations are carried out by using the program FEFF8 (version 8.2),[91] and the resulting simulated spectra are directly compared to readily available experimental data.[36,38]

3. Results and Discussion

The results are presented in eight subsections. Section 3.1 describes QM/MM models of the OEC of PSII in the S_1 state that are consistent with a broad range of experimental data. The electronic and structural properties of the models, introduced in section 3.1, are analyzed in sections 3.2 and 3.3, respectively. Section 3.4 analyzes the coordination of

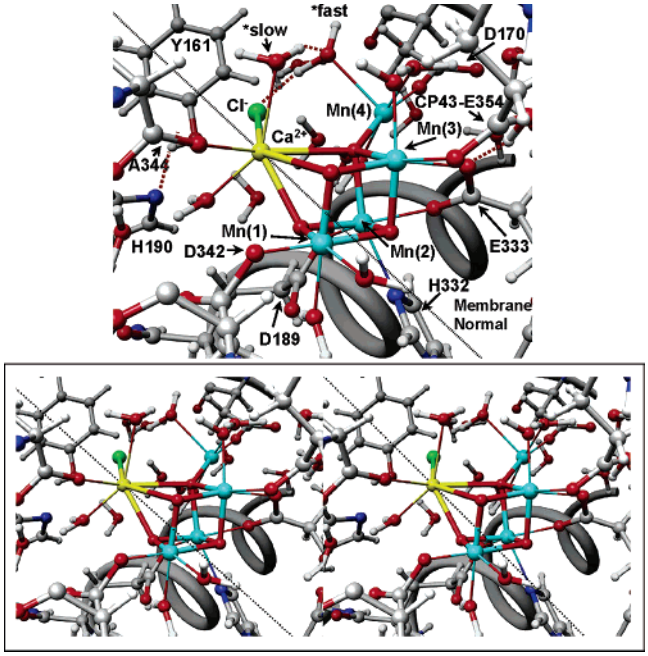

Figure 6. DFT QM/MM minimum energy geometry of the OEC of PSII, obtained at the ONIOM-EE (UHF B3LYP/lacvp,6-31G(2df),6-31G:AMBER) level of theory. Upper and lower panels show the OEC and surrounding residues in mono- and stereoviews, respectively. Putative substrate waters are labeled *slow and *fast (see text for explanation). Note that all amino acid residues correspond to the D1 protein subunit, unless otherwise indicated.

the oxomanganese complex by substrate water molecules in the presence of Ca^{2+} and Cl^- ions. The positioning of amino acid residues D1-Y161 and CP43-R357, relative to the oxomanganese complex, is discussed in section 3.6. The effect of oxidation and reduction of the OEC of PSII is analyzed in section 3.7 in terms of the resulting structural and electronic rearrangements as compared to readily available experimental data. Finally, section 3.8 describes a family of molecular structures, closely related to the QM/MM models discussed in sections 3.1−3.7, that are found to be also largely consistent with a wide range of experiments.

3.1. QM/MM Structural Models. Several QM/MM structural models have good agreement with the X-ray structure of Ferreira et al.,[4] differing only in the protonation states, or number of ligated water molecules, or the coordination of labile ligands. However, only two combinations of spin states were found for the S_1 resting state. These include model **A**, with Mn_4(IV,IV,III,III) or Mn(1) = IV, Mn(2) = IV, Mn(3) = III, Mn(4) = III, in which the dangling manganese is pentacoordinated, and model **B**, with Mn_4(IV,III,III,IV), in which the dangling manganese has an additional ligated water molecule completing the six-coordination shell.

Figure 6 shows model **A**, a fully relaxed QM/MM structural model of the OEC of PSII in the S_1 resting state Mn_4(IV,IV,III,III), obtained at the ONIOM-EE (UHF B3LYP/lacvp,6-31G(2df),6-31G:AMBER) level of theory, including complete ligation of the Mn tetramer. Model **B** includes an additional water molecule ligated to the dangling Mn(4) that completes the hexacoordination of the dangling manganese in the stabilization of a high-valent oxidation state IV. Because of the slightly strained coordination of D1-H332 to Mn(2) in the Mn cluster, the hexacoordination of Mn(2) becomes less favorable when the coordination sphere of Mn(4) is complete, and this stabilizes an oxidation state III for Mn(2), with a Jahn−Teller elongation along the Mn−N(D1-H332) axis. Therefore, the resulting state is Mn_4(IV,III,III,IV).

Note that, in contrast to the 1S5L structure (see Figure 3), Mn ions with oxidation states III and IV have the usual number of coordinated ligands (i.e., five or six, respectively) and Ca^{2+} has seven ligands. The QM/MM ligation of amino acid residues, however, is slightly different from the ligation scheme suggested by the X-ray diffraction structure.[4] The proteinaceous ligation in the QM/MM models includes η^2 coordination of D1-E333 to both Mn(3) and Mn(2) and hydrogen bonding to the protonated (neutral) state of CP43-E354; monodentate coordination of D1-D342, CP43-E354, and D1-D170 to Mn(1), Mn(3), and Mn(4), respectively; and ligation of D1-E189 and D1-H332 to Mn(2).

Table 1 presents a comparative analysis of interatomic bond lengths and bond orientation angles relative to the membrane normal, including models **A** and **B**, obtained at the ONIOM-EE (UHF B3LYP/lacvp,6-31G(2df),6-31G:AMBER) level of theory, the X-ray diffraction structure 1S5L, solved at 3.5 Å resolution,[4] EXAFS data,[54] and a reduced model system in the absence of the surrounding protein environment.[77] It is shown that the configuration of the cuboidal Mn_3CaO_4Mn complex in both QM/MM hybrid models is very similar to the structural model proposed by Ferreira et al.[4] In fact, for both models, the root-mean-squared displacement of the QM/MM structural models, relative to the X-ray diffraction structure, is 0.6 Å. Therefore, it is difficult to judge whether the oxomanganese complex in the QM/MM models and 3.5 Å resolution X-ray structure are truly identical or whether there are any significant differences. In addition, as discussed in sections 3.2−3.8, the underlying structural and electronic properties of the QM/MM model are found to be in very good agreement with a wide range of experimental data of PSII. Furthermore, the comparison presented in Table 1 also indicates that there are only minor structural rearrangements in the oxomanganese complex when the configuration of the system is relaxed after substituting the surrounding protein environment by a reduced model with ligands that mimic the proteinaceous chelation scheme introduced by the QM/MM hybrid model.[77]

These results suggest that the proposed cuboidal model of the inorganic core of the OEC of PSII, completely ligated with water, OH^-, and Cl^- and proteinaceous ligands, is a stable molecular structure not only in two possible states (models **A** and **B**) associated with a slightly different coordination of the dangling Mn(4) but also in the absence of the surrounding protein environment.[77] Therefore, it is expected that significant insight could be provided by reduced model systems once the proteinaceous chelation scheme is elucidated by applying QM/MM hybrid methods in conjunction with moderate-resolution X-ray diffraction structures.

Considering the structural similarities between the cuboidal Mn_3CaO_4Mn complexes in the reduced model and those in the QM/MM hybrid structures, it is natural to conjecture that

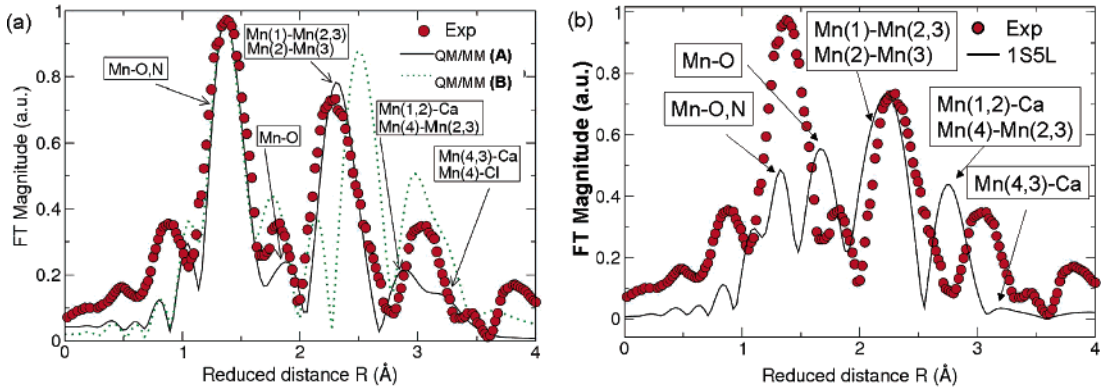

Figure 7. Comparison between the experimental EXAFS spectrum of the OEC of PSII in the S_1 state (red dots)[36,38] and the calculated EXAFS spectra for (a) the DFT QM/MM models and (b) the X-ray diffraction structure.

Table 1. Interatomic Bond Lengths and Bond Orientation Angles (Relative to the Membrane Normal) in DFT-QM/MM Structural Models **A** and **B** of the OEC of PSII in the S_1 State (Described in the Text), Including Comparisons to the X-ray Diffraction Structure,[4] EXAFS Data,[54] and the Configuration of the Reduced Quantum Mechanical Model in the Absence of the Protein Environment[77]

	bond lengths					bond angles		
bond vector	**A**	**B**	X-ray	EXAFS[a]	red. model[b]	**A**	**B**	X-ray
Mn(1)−Mn(2)	2.76 Å	2.71 Å	2.65 Å	2.7 Å	2.77 Å	57°	59°	59°
Mn(1)−Mn(3)	2.76 Å	2.75 Å	2.67 Å	2.7 Å	2.76 Å	85°	82°	79°
Mn(2)−Mn(3)	2.82 Å	2.78 Å	2.72 Å		2.87 Å	63°	65°	71°
Mn(2)−Mn(4)	3.34 Å	3.79 Å	3.25 Å	3.3 Å	3.42 Å	54°	49°	58°
Mn(3)−Mn(4)	3.72 Å	3.61 Å	3.26 Å		3.74 Å	29°	24°	38°
Ca−Mn(2)	3.31 Å	3.41 Å	3.40 Å	3.4 Å	3.42 Å	53°	55°	59°
Ca−Mn(3)	3.95 Å	3.61 Å	3.38 Å		3.51 Å	35°	38°	39°

[a] EXAFS data[54] include only two Mn−Mn distances of 2.7 Å, one Mn−Mn distance of 3.3 Å, and one Ca−Mn distance of 3.4 Å. [b] Interatomic distances in a reduced quantum mechanical model of the OEC computed at the UB3LYP level of theory.[77]

the biomolecular environment must conform to the intrinsic properties of the ligated inorganic oxomanganese core, achieving catalytic functionality simply by positioning suitable sources and sinks of electrons and protons. The extent to which these results are significant is associated with the intrinsic limitations of moderate resolution X-ray diffraction models, obtained under conditions of unavoidable photoreduction of Mn ions and the rapid exchange of labile substrate ligands.

3.2. Mn−Mn Distances: EXAFS Spectra. In contrast to the symmetric configuration of the X-ray diffraction model of the OEC of PSII (PDB access code 1S5L),[4] with three Mn−Mn distances of about 2.7 Å, the DFT QM/MM hybrid models described in section 3.1 suggest that the S_1 state of the OEC has two short Mn−Mn distances of 2.71−2.76 Å per Mn tetramer (one of which is oriented at about 60° relative to the membrane normal), one slightly longer Mn−Mn distance of 2.78−2.82 Å, one ∼3.3 Å Mn−Mn distance, and one ∼3.3−3.4 Å Mn−Ca distance.[92] These results are roughly consistent with most XAS data, often interpreted in terms of two 2.7 Å vectors per Mn_4 complex oriented at 60°[33,93,94] (79°).[55] This important structural feature, however, remains controversial.[36] In fact, it has been proposed that there might be three Mn−Mn vectors of 2.7−2.8 Å per Mn_4 complex already in the S_1 state.[37]

To make direct comparisons with readily available XAS experimental data, Figure 7a compares the simulated spectra of the DFT QM/MM models **A** and **B** and the experimental EXAFS spectrum of the OEC of PSII in the S_1 state (red dots).[36,38] The simulations are based on the real space Green's function methodology described in Section 2.4. It is shown that the simulated EXAFS spectrum of **A** is in very good agreement with experimental data, including the description of the widths and positions of multiscattering peaks associated with Mn−ligand distances of ∼1.8 Å (reduced distance of ∼1.6 Å) and Mn−Mn distances of ∼2.7 Å (reduced distance of ∼2.5 Å). In contrast, the simulated EXAFS spectrum based on the X-ray diffraction model (see Figure 7b) is in much worse agreement with the experimental EXAFS spectrum. This disagreement is partly due to the different proteinaceous ligation scheme and the incomplete coordination of metal ions in the cluster. The discrepancies in model **B** are due to inequivalent Mn−Mn distances, splitting a single peak at a reduced distance of ∼2.5 Å into a bimodal structure.

3.3. Electronic Structure of the S_1 State. Table 2 shows that the DFT−QM/MM hybrid models predict high-valent configurations of the S_1 state of the OEC of PSII, with oxidation numbers Mn_4(IV,IV,III,III) and Mn_4(IV,III,III,IV) for model structures **A** and **B**, respectively. These results are consistent with EPR and X-ray spectroscopic evidence[55,94−99] but disagree with low-valent Mn_4(III,III,III,III) proposals.[100,101]

Table 2 indicates that both models **A** and **B** involve antiferromagnetic coupling between Mn(1) and Mn(2), between Mn(2) and Mn(3), and between Mn(3) and Mn(4)

Table 2. Formal Oxidation Numbers, Mulliken Spin-Population Analysis, and ESP Atomic Charges in the QM/MM Models of the OEC of PSII in the S_1 State

	oxidation #		spin population		ESP charge	
ion center	**A**	**B**	**A**	**B**	**A**	**B**
Mn(1)	+4	+4	+2.80	+2.81	+1.11	+1.16
Mn(2)	+4	+3	−2.75	−3.84	+1.08	+1.43
Mn(3)	+3	+3	+3.82	+3.82	+1.26	+1.30
Mn(4)	+3	+4	−3.80	−2.80	+1.35	+1.41
Ca	+2	+2	−0.01	+0.01	+1.77	+1.60
O(5),O(6)	−2, −2	−2, −2	−0.00, −0.02	+0.02, −0.01	−0.60, −0.80	−0.71, −0.89
O(7),O(8)	−2, −2	−2, −2	+0.08, −0.07	−0.04, +0.04	−0.67, −0.98	−0.64, −1.14

but frustrated coupling between Mn(1) and Mn(3). It is important to note, however, that predicting the correct relative stability of low-lying spin states in multinuclear oxomanganese complexes might be beyond the capabilities of the implemented DFT/B3LYP methodology.[77] For completeness, Table 2 compares the formal oxidation numbers (columns 2 and 3) as determined by the spin-population analysis (columns 4 and 5) to the actual ESP atomic charges (columns 6 and 7) of the corresponding ions. It is shown that the relation between oxidation numbers and atomic charges is complicated by the fact that there is charge transfer between bridging oxygen and manganese ions, similar to charge delocalization mechanisms observed in synthetic oxomanganese complexes.[77] Therefore, it is natural to expect that rationalizing certain properties of the oxomanganese complex of the OEC of PSII, such as ligand-exchange rates and the effect of changes in oxidation states on the vibrational spectroscopy of specific ligands,[42−44] might require a complete electronic analysis in which both atomic charges and Mulliken spin populations are considered. Otherwise, these properties might be difficult to interpret by using an analysis based solely on formal oxidation numbers. As an example, Table 2 shows that the atomic charge of Ca^{2+} of model **A** (+1.77), with a formal oxidation number of II, is higher than the atomic charges of Mn^{3+} and Mn^{4+} (1.08−1.35; with oxidation numbers III and IV, respectively), suggesting that Ca^{2+} with its smaller oxidation number may actually bind the *slowly* exchanging substrate water molecule, in agreement with experimental observations.[72]

3.4. Substrate Water Binding. The QM/MM hybrid models rationalize the 1S5L electronic density, initially assigned to bicarbonate (see Figure 3), to substrate water molecules bound to Mn(4) and Ca^{2+} (see Figure 6). This arrangement is consistent with mechanistic proposals,[4,5,14,19,21] because the respective substrate oxygen atoms are 2.72 Å apart and may be brought yet closer together in the S_4 state (following deprotonation of the Mn-bound water) to achieve O−O bond formation in the $S_4 \rightarrow S_0$ transition. Further, hydration of the cluster is broadly in line with pulsed EPR experiments which reveal the presence of several exchangeable deuterons near the Mn cluster in the S_0, S_1, and S_2 states.[23] However, the number of water molecules ligated to Mn ions is larger than would be expected from the analysis of exchangeable deuterons, as observed in pulsed EPR studies.[23] Therefore, the substitution of ligated water molecules by bicarbonate elsewhere in the OEC[19,102] cannot be discounted. In the absence of bicarbonate, however, models constructed by completing the Mn coordination numbers according to the principle of *minimum number of additional water molecules* have been dismissed, because such structures require unrealistic displacements of the ligating amino acid residues relative to their corresponding positions in the crystallographic 1S5L structure.[13,14]

Possible binding positions for bicarbonate have been analyzed in the DFT−QM/MM hybrid models, including (i) bidentate coordination to Mn(1), (ii) chelation between Mn(3) and Mn(4), and (iii) coordination to Mn(4) and calcium (analogous to Ferreira's X-ray structure). In each case, bicarbonate replaces two water molecules (or a water molecule and a hydroxide ligand) bound to the OEC model, as shown in Figure 6. It is found that, in the first ligation scheme (i.e., case i), bicarbonate ligates by splitting into CO_2 and OH^- (the C−O distance is 0.4 Å longer than the equilibrium value in vacuo). In the second and third schemes (i.e., cases ii and iii), the resulting structure is stable. However, higher-resolution crystal structures[51,52] have not corroborated the presence of bicarbonate. Further, it has been recently shown that bicarbonate is not the substrate.[103] Therefore, bicarbonate has not been included in the proposed QM/MM structural models **A** and **B**.

3.5. Chloride Binding. The QM/MM hybrid models include a calcium-bound chloride ion (see Figure 6): Cl^- is 3.1 Å from Ca^{2+} and 3.2 Å from the phenoxy oxygen of D1-Y161. Such an arrangement of ligands completes a coordination sphere of seven ligands for Ca^{2+} (often chelated by up to eight ligands), including Cl^-, two water molecules, the monodentate carboxylate terminus of D1-A344, and the three bridging oxides of the cuboidal structure.

The presence of the chloride ion has not been resolved by X-ray diffraction experiments. However, the binding site suggested by the QM/MM hybrid models is consistent with the experimental observation that acetate binds competitively with chloride[104] and blocks catalysis at the S_2 state.[105] It has also been suggested that chloride is required for transitions beyond the S_2 state.[105] Furthermore, the direct binding of chloride to calcium is consistent with the proposal that chloride is part of a proton relay network.[106] In addition, the QM/MM models are consistent with pulsed EPR experiments of the OEC in which chloride has been replaced by acetate, revealing a distance of 3.1 Å from the methyl deuterons of the bound acetate to the phenoxy oxygen of D1-Y161.[107]

The chloride/acetate substitution has been analyzed in the QM/MM computational models, to partially validate the proposed Cl^- binding site. The chloride/acetate substitution

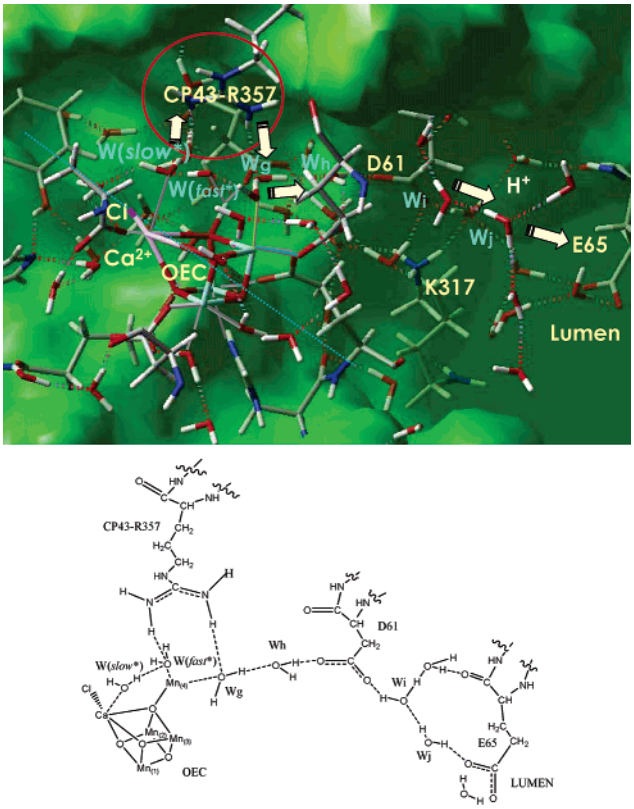

Figure 8. Proton exit channel toward the lumenal surface of the membrane, suggested by the DFT QM/MM structural models, involving an extended network of hydrogen bonds from the substrate water molecules W_s and W_f to CP43-R357 and from CP43-R357 to D1-D61, which is the first residue of the putative proton-transfer channel leading to the lumenal surface of PSII via hydrogen-bonded water molecules W_g, W_h, W_i, and W_j. Note that all amino acid residues correspond to the D1 protein subunit, unless otherwise indicated.

required the removal of two water molecules (originally coordinated to Ca^{2+}) in order to avoid strong repulsive interactions. The removal of bound water molecules is consistent with the experimental evidence that adding acetate to the OEC displaces several water molecules from the protein cavity.[108] After geometry optimization, the carboxylate group of acetate replaces Cl^- and the C−C bond becomes collinear with the previously modeled Cl^-−Ca^{2+} bond. Furthermore, the phenoxy oxygen of D1-Y161 is found to be 3.2 Å from the averaged position of the acetate methyl hydrogens (3.1 Å from the methyl carbon), in excellent agreement with experimental observations.

3.6. Function of D1-Y161 (Y_Z) and CP43-R357. Tyrosine D1-Y161 has long been viewed as an electron-transport cofactor. As mentioned in section 1, the oxidized state $P680^+$ is thought to be reduced by the redox-active tyrosine D1-Y161 (Y_Z), which is in turn reduced by an electron from the OEC.[109,110] The QM/MM structural models of PSII seem to be consistent with such a postulated redox mechanism, especially judging by the proximity of Y_Z to the Mn cluster, although this remains to be demonstrated by rigorous calculations of redox potentials, which we will present elsewhere. Simple inspection of the QM/MM structural models (see Figure 8), however, reveals that the phenoxy oxygen of Y_Z is close to the chloride ligand (3.4 Å) and that the Ca^{2+}−Cl^- bound length is 3.14 Å. Furthermore, the QM/MM structure shown in Figure 8 indicates that the Y_Z phenol group is hydrogen-bonded to the imidazole ϵ-N of the D1-H190 side chain (see also Figure 6). This hydrogen-bonding partnership is consistent with mutational and spectroscopic studies[45,111,112] as well as with earlier studies based on MM models.[13,14]

The possibility that the oxidized Y_Z radical might simultaneously oxidize and deprotonate the hydrated OEC[113] would require a mechanism in which Y_Z abstracts hydrogen atoms and delivers protons to the protein surface via D1-H190. However, on the basis of the lack of a H-bonding pathway leading from D1-H190 to the lumen, it is more likely that D1-H190 accepts a proton from Y_Z during the oxidation of Y_Z and returns the proton to Y_Z upon its reduction. Consistently, the QM/MM structural models suggest that other amino acid residues (e.g., CP43-R357) might be more favorably placed for proton abstraction,[13,14,19] because substrate water molecules are not directly exposed to Y_Z.

The QM/MM hybrid models show that a network of hydrogen bonds is formed around the catalytically active face of the OEC cluster (see Figure 8), including both substrate water molecules, the side chain of CP43-R357, and the calcium-bound chloride ion. Nearby, two hydrogen-bonded nonligating water molecules are found to fit easily into the structure between Mn(4) and D61, the first residue of the putative proton-transfer channel leading to the lumenal surface of PSII. The proximity of CP43-R357 to the Mn cluster in the QM/MM hybrid models suggests that CP43-R357 might play the role of the redox-coupled catalytic base in the latter half of the S-state cycle.[19] A recent computational study indicates that the pK_a of D1-R357 is indeed particularly sensitive to an increase in the charge of the Mn/Ca cluster.[114] We will present our calculations of pK_a values of acid/base groups along the proton exit channel elsewhere. It is expected that a pK_a gradient along the channel should facilitate proton transfer into an entropically favored (i.e., irreversible) state in the lumenal bulk solution.

3.7. S_0 and S_2 States. The DFT−QM/MM hybrid models of the OEC of PSII in the S_1 state, reported in previous sections, allow for the investigation of structural changes induced by oxidation/reduction of the OEC and the effect of such electronic changes on the underlying ligation scheme. The $S_1 \rightarrow S_2$ transition involves oxidation[115−117] without deprotonation. This can be achieved by the oxidation of one of the two manganese ions with oxidation state III [i.e., Mn(3) or Mn(4), in model **A**, and Mn(2) or Mn(3), in model **B**].

Minimum-energy structures, obtained by optimizations initialized with both possible spin configurations for each model, indicate that the more likely configurations involve the oxidation of Mn(3) in model **A** and the oxidation of Mn(2) in model **B** (see Table 3 and Figure 9).

Therefore, DFT QM/MM models **A** and **B** predict that the S_2 state, obtained at the ONIOM-EE (UHF B3LYP/lacvp,6-31G(2df),6-31G:AMBER) level of theory, involves the high-valent configuration Mn_4(IV,IV,IV,III) or

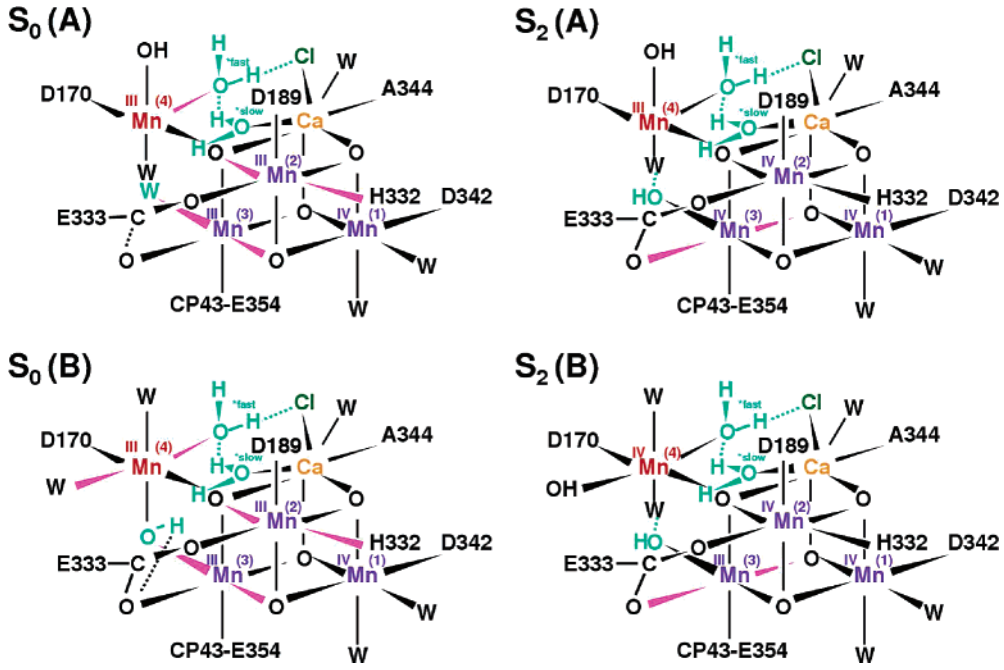

Figure 9. Schematic representation of the proteinaceous ligation scheme in the DFT QM/MM models **A** and **B** of the OEC of PSII in the S_0 (left panel) and S_2 (right panel) states. Elongated bonds due to Jahn−Teller distortion are represented in magenta. Note that all amino acid residues correspond to the D1 protein subunit, unless otherwise indicated.

Table 3. Mulliken Spin Population Analysis and ESP Atomic Charges in the DFT QM/MM Models of the OEC of PSII in the S_0 and S_2 States

	S_0						S_2					
	spin population		oxidation #		ESP charge		spin population		oxidation #		ESP charge	
ion center	**A**	**B**	**A**	**B**	**A**	**B**	**A**	**B**	**A**	**B**	**A**	**B**
Mn(1)	−2.75	−2.86	+4	+4	+1.41	+1.33	−2.79	−2.76	+4	+4	+1.14	+1.25
Mn(2)	+3.76	+3.78	+3	+3	+1.36	+1.35	+2.92	+3.15	+4	+4	+1.02	+1.52
Mn(3)	−3.81	−3.85	+3	+3	+1.43	+1.33	−2.74	−3.82	+4	+3	+1.59	+1.11
Mn(4)	+3.76	+3.82	+3	+3	+1.39	+1.47	+3.79	+3.17	+3	+4	+1.49	+1.50
O(5)	0.00	−0.03	−2	−2	−0.75	−0.60	+0.09	−0.07	−2	−2	−0.53	−0.78
O(6)	−0.04	−0.07	−2	−2	−0.99	−0.86	+0.02	−0.01	−2	−2	−0.81	−0.80
O(7)	+0.08	+0.03	−2	−2	−0.75	−0.73	−0.03	−0.03	−2	−2	−0.78	−0.67
O(8)	−0.04	+0.01	−2	−2	−1.14	−1.14	−0.09	−0.05	−2	−2	−0.86	−1.22
Ca	−0.00	−0.00	+2	+2	+1.62	+1.62	−0.00	−0.02	+2	+2	+1.56	+1.66
Cl	−0.00	−0.00	−1	−1	−0.77	−0.75	+0.00	+0.28	−1	−1	−0.67	−0.41

Table 4. Interionic Distances and Bond Angles, Relative to the Membrane Normal, in the DFT QM/MM Structural Models of the OEC of PSII in the S_0 and S_2 States

	S_0				S_2			
	bond length		bond angle		bond length		bond angle	
bond vector	**A**	**B**	**A**	**B**	**A**	**B**	**A**	**B**
Mn(1)−Mn(2)	2.70 Å	2.70 Å	58°	58°	2.78 Å	2.71 Å	58°	58°
Mn(1)−Mn(3)	2.78 Å	2.91 Å	82°	82°	2.76 Å	2.73 Å	81°	81°
Mn(2)−Mn(3)	2.78 Å	2.92 Å	68°	68°	2.86 Å	2.79 Å	65°	65°
Mn(2)−Mn(4)	3.52 Å	3.59 Å	58°	58°	3.31 Å	3.79 Å	59°	59°
Mn(3)−Mn(4)	3.43 Å	2.94 Å	32°	32°	3.55 Å	3.67 Å	35°	35°
Ca−Mn(2)	3.40 Å	3.51 Å	57°	57°	3.78 Å	3.36 Å	57°	57°
Ca−Mn(3)	3.71 Å	3.52 Å	38°	38°	3.98 Å	3.77 Å	36°	36°

Mn_4(IV,IV,III,IV). The analysis of the configurations of the relaxed S_1 and S_2 QM/MM hybrid models (see Tables 1 and 4) indicates that the $S_1 \rightarrow S_2$ oxidation is not expected to involve any significant rearrangement of ligands, or structural changes in the Mn cluster (Table 4). These results are, thus, in agreement with recent findings of EXAFS studies.[38]

The $S_0 \rightarrow S_1$ transition involves the oxidation of a manganese ion and the deprotonation of a ligand (probably

a water molecule[5,14] or bridging oxide[38]), a process that induces structural rearrangements in the oxomanganese cluster, shortening a Mn−Mn distance by approximately 0.15 Å.[37]

To elucidate the nature of the S_0 state and the specific electronic and structural changes induced upon oxidation of the system, several DFT QM/MM hybrid models have been investigated. The analysis of QM/MM structures indicates that Mn(2) is oxidized in model **A**, and Mn(4) is oxidized in model **B**, during the $S_0 \rightarrow S_1$ step (see Tables 2 and 3). Therefore, both DFT QM/MM models, obtained at the ONIOM-EE (UHF B3LYP/lacvp,6-31G(2df),6-31G:AMBER) level of theory, predict that the S_0 state has the high-valent configuration Mn_4(IV,III,III,III).

Considering that the proposed DFT QM/MM hybrid model does not involve the protonation of bridging oxides, the potential ligands responsible for deprotonation are water molecules ligated to Mn(3) or Mn(4), because Mn(2) has no water ligands and changes in protonation states of water molecules ligated to Mn(1) would not involve changes in the active site of the cluster. In particular, model **A** suggests that a water molecule ligated to Mn(3) is the best candidate because the ligated molecule is deprotonated (HO^-) in the S_1 state, while model **B** points to deprotonation of a water molecule ligated to Mn(4).

Table 4 summarizes the configurations of models **A** and **B** in the S_0 state, indicating that the DFT QM/MM hybrid models predict a single 2.7 Å Mn−Mn distance per Mn tetramer (oriented at about 58° relative to the membrane normal), which is 0.06 Å shorter than that in the S_1 state. Furthermore, the QM/MM models of the S_0 state indicate that the Jahn−Teller effect in Mn(3) elongates the distance Mn(1)−Mn(3), making it slightly longer than the distance Mn(1)−Mn(2). This effect is more pronounced in model **B** than in model **A**, because in model **B** the elongation is along the direction of the μ-oxo bridge linking Mn(3)−Mn(1) and Mn(3)−Mn(2). In contrast, model **A** involves elongation along the coordination axis with D1-E333. Such a distortion is also responsible for moving the D1-E333 ligand away from Mn(3), partially forming an oxo-bridge with Mn(4) (see Figure 9).

3.8. Ligation of D1-E333. The 1S5L crystal structure indicates that the amino acid residue D1-E333 is ligated at an intermediate position between Mn(2) and Mn(4), with its carboxylate group in close contact with the carboxylate side-chain of CP43-E354. The QM/MM analysis of the OEC of PSII in the S_1 state indicates that the intrinsic stability of the pair of amino acid residues D1-E333 and CP43-E354, in close contact with each other, is not only due to coordination to the oxomanganese complex but also due to hydrogen bonding between the protonated (neutral) CP43-E354 and the carboxylate group of D1-E333.

Several other ligation schemes for the amino acid residue D1-E333 have been analyzed in an effort to investigate the influence of chelation on the geometry of the OEC cluster in the S_1 state. Relevant geometrical parameters for fully optimized QM/MM models, with ligation schemes depicted in Figure 10, are reported in Table 5.

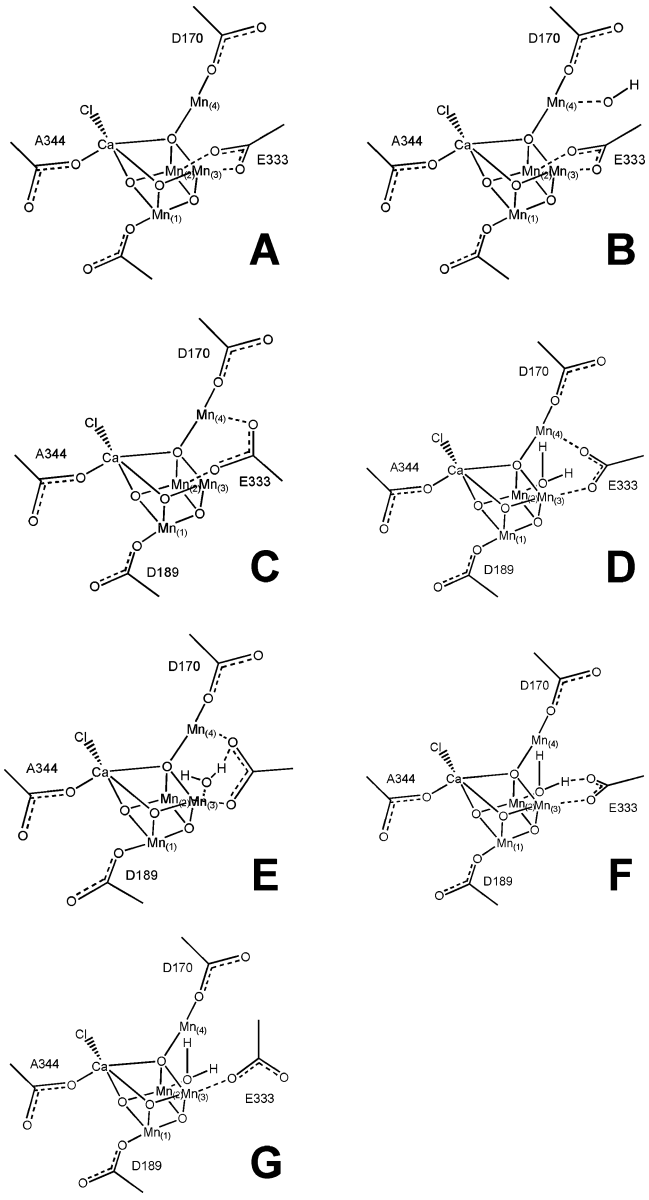

Figure 10. Possible ligation schemes for the carboxylate terminus of amino acid residue D1-E333 and a water molecule ligated to the OEC of PSII. Note that all amino acid residues correspond to the D1 protein subunit, unless otherwise indicated.

Schemes A and B correspond to the QM/MM structures **A** and **B**, introduced in section 3.1. These structures involve η^2 coordination of D1-E333 to Mn(2) and Mn(3). Scheme C involves D1-E333 chelation to both Mn(4) and Mn(2), with a minimum displacement of the side chain of D1-E333 relative to the X-ray configuration. Schemes D−F correspond to D1-E333 coordination to Mn(2) or Mn(3), competing with a water molecule for the other metal center. It is found that all of the ligation schemes described in Figure 10 are within the resolution limits of the X-ray structure because the displacement of each carboxylate oxygen is smaller than 1 Å, relative to their configuration in the X-ray structure.

Direct comparisons between the resulting structural models obtained with each of these possible ligation schemes and readily available EXAFS data are not straightforward. On the basis of EXAFS studies, it was initially concluded that

Table 5. Interionic Distances in the OEC of PSII in the S_1 State for Different Ligation Schemes of the Amino Acid Residue D1-E333

ref.[a]	scheme[b]	1−2[c]	1−3[c]	2−3[c]	2−4[c]	3−4[c]	Ca-2[c]	Ca-3[c]
A(1)	2−3	2.76 Å	2.76 Å	2.82 Å	3.34 Å	3.72 Å	3.31 Å	3.95 Å
A(2)	2−3 + OH(4)[d]	2.70 Å	2.73 Å	2.80 Å	3.79 Å	3.66 Å	3.34 Å	3.44 Å
B	2−4	2.76 Å	2.77 Å	3.00 Å	3.27 Å	3.68 Å	3.49 Å	3.42 Å
C	3−4 + w(2)[e]	2.79 Å	2.73 Å	2.86 Å	3.61 Å	3.59 Å	3.10 Å	4.20 Å
D	w(3)−2−4[f]	2.75 Å	2.79 Å	3.02 Å	3.40 Å	3.89 Å	3.37 Å	3.68 Å
E	w(2)−3	2.77 Å	2.76 Å	3.01 Å	3.14 Å	3.64 Å	3.19 Å	4.37 Å
F	3 + w(2)	2.79 Å	2.78 Å	2.93 Å	2.95 Å	3.49 Å	3.12 Å	4.44 Å

[a] Schemes are labeled according to Figure 10. [b] Atom numbers correspond to the Mn center to which Glu333 is ligated; w(#) or OH(#) indicate a water molecule or OH^-, respectively, ligated to Mn(#), see Figure 10. [c] For simplicity, Mn symbols in table headers are omitted, e.g., 1−2 stands for Mn(1)−Mn(2), etc. [d] The oxidation state is Mn_4(IV,III,IV,III). [e] The optimization of the structure without a water ligated to Mn(2) (i.e., 3−4) converged to 2−3.

the S_1 state has two 2.7 Å Mn−Mn distances, one 3.3−3.4 Å Mn−Ca distance, and one 3.3 Å Mn−Mn distance.[118] However, it was recently reported that a third 2.7 Å Mn−Mn distance may be present.[37,54] Dau et al.[38] reported that a third, longer Mn−Mn distance of about 2.8 Å might also be present, but this was disfavored because its inclusion lowered the fit quality of the EXAFS spectrum simulations.[36] Furthermore, there also seems to be no agreement on the number of 3.3−3.4 Å Mn−Ca distances, reported as one or two 3.4 Å distances by the Berkeley group[54] and two or three 3.3 Å distances by the Berlin group.[38]

All structures in Table 1 show two short Mn−Mn distances and a third Mn−Mn distance that is longer by 0.06−0.17 Å. The calculations also show one Mn−Ca distance and one Mn−Mn distance of ca. 3.3 Å, consistent with both the Berkeley and Berlin groups' EXAFS analyses. Accordingly, all ligation schemes show qualitative accordance with the number and relative magnitudes of Mn−Mn and Mn−Ca distances proposed by both experimental groups. In particular, the coordination scheme that includes the ligation of D1-E333 to Mn(2) and Mn(3) has the smallest "long" Mn−Mn distance (2−3 in Table 1), making the three Mn−Mn distances lie within the uncertainty of the DFT QM/MM method. In this way, the models introduced in sections 3.1−3.7 are consistent with a whole set of measurements, both of the Berkeley group and of the Berlin group. The other possibilities discussed in this section, however, cannot be ruled out on either experimental or current computational grounds.

Other possible QM/MM structures have been analyzed, differing in the protonation state of ligated water molecules or in the coordination of labile ligands. For simplicity, however, the presentation has been limited to the fully optimized QM/MM models whose structural features are most consistent with EXAFS measurements.

4. Conclusions

We have developed chemically sensible structural models of the OEC of PSII with complete ligation of the metal-oxo cluster by amino acid residues, water, hydroxide, and chloride. The models were developed at the DFT QM/MM ONIOM-EE (UHF B3LYP/lacvp,6-31G(2df),6-31G:AMBER) level of theory. Manganese and calcium ions are ligated consistently with standard coordination chemistry assumptions, supported by much biochemical and spectroscopic data, including a calcium-bound chloride ligand which is docked consistently with pulsed EPR data obtained from acetate-substituted PSII. Proteinaceous ligation includes the monodentate coordination of D1-D342, CP43-E354, and D1-D170 to Mn(1), Mn(3), and Mn(4), respectively; the coordination of D1-E333 to both Mn(3) and Mn(2) and hydrogen bonding of D1-E333 to CP43-E354, which is in the protonated (neutral) form; and the ligation of D1-D189 and D1-H332 to Mn(2). The proposed models are found to be stable and entirely consistent with available mechanistic data as well as compatible with EXAFS measurements and X-ray diffraction models of PSII (i.e., with root-mean-squared displacement smaller than 1 Å relative to the X-ray structure). Therefore, it is concluded that the proposed QM/MM structures are particularly relevant to the investigation and validation of reaction intermediates of photosynthetic water oxidation.

We have found a family of closely related QM/MM structural models which are partially consistent with a wide range of experiments. Most of these structures differ only in the protonation state of water molecules ligated to the Mn cluster, or in the coordination of a proteinaceous ligand (D1-E333). It is, therefore, concluded that the intrinsic degeneracy of protonation states and coordination patterns (as well as low-lying spin states) might be necessary to ensure the robustness of the functionality in the presence of thermal fluctuations.

We have found that the DFT QM/MM level of theory predicts high-valent electronic configurations with oxidation numbers Mn_4(III,III,III,IV) for the S_0 state, Mn_4(III,IV,IV,IV) for the S_2 state, and Mn_4(III,III,IV,IV) or Mn_4(IV,III,III,IV) for the S_1 state, consistent with EPR and X-ray spectroscopic evidence.[55,94−99] However, we caution that further studies exploring the relative stability of different spin states are required, because predicting the correct relative stability of low-lying spin states in multinuclear oxomanganese complexes might be beyond the current capabilities of the DFT B3LYP hybrid functional.[77] This problem adds one more example to the list of high-valent transition-metal complexes in which DFT might provide an unreliable description of the energetics of the low-lying spin-electronic states.[119−125]

In agreement with experiments,[38] we found that the $S_1 \rightarrow S_2$ oxidation does not involve any significant rearrangement of ligands, or structural changes in the Mn cluster. In contrast, the $S_0 \rightarrow S_1$ oxidation step deprotonates a water molecule

ligated to Mn(3) and oxidizes Mn(2) from III to IV in model **A** or oxidizes Mn(4) and deprotonates a water molecule ligated to Mn(4) in model **B**. The resulting Jahn−Teller effect in the S_0 state elongates the Mn(1)−Mn(3) distance relative to Mn(1)−Mn(2). In agreement with EXAFS experiments, the proposed DFT−QM/MM structures predict that the S_0 state involves a single Mn−Mn vector close to 2.7 Å.

We conclude that the relation between oxidation numbers and atomic charges is complicated by charge transfer between μ-O and Mn ions, similar to charge delocalization mechanisms observed in synthetic oxomanganese complexes.[77] Therefore, we found that joint charge- and spin-population analysis might be necessary in order to rationalize certain mechanistic and structural properties of the system, including water exchange rates and the vibrational spectroscopy of ligated residues. In fact, in agreement with experimental measurements of exchange rates, the charge-population analysis indicates that Ca^{2+} carries the highest positive charge and, therefore, might bind the slow exchanging substrate water molecule, even though its formal oxidation number is smaller than that of the dangling manganese.

We have found that the proximity of D1-Y161 (Y_Z) to the Mn cluster in the QM/MM structural model of PSII is consistent with the electron-transfer role of D1-Y161 (Y_Z). However, the actual calculation of redox potentials will be necessary to address this fundamental aspect. These calculations involve work in progress in our group and will be presented elsewhere. In particular, the synergistic modulation of protonation and redox states will be addressed in terms of continuum electrostatic calculations based on the DFT QM/MM molecular structures reported herein. Furthermore, we have found that the substrate water molecules are directly exposed to CP43-R357 in the QM/MM structural models. We found an extended network of hydrogen bonds linking CP43-R357 with D1-D61, suggesting a proton exit channel toward the lumenal surface of the membrane.

We have found only minor structural rearrangements in the oxomanganese complex after substituting the surrounding protein environment by a reduced model with ligands that mimic the proposed QM/MM proteinaceous ligation scheme. These results suggest that the cuboidal model of the inorganic core of the OEC of PSII, completely ligated with water, OH^-, Cl^- and proteinaceous ligands, is a stable molecular structure even in the absence of the surrounding protein environment. Therefore, it is natural to conjecture that the biomolecular environment must conform to the intrinsic properties of the ligated inorganic oxomanganese complex, achieving catalytic functionality simply by positioning suitable sources and sinks of electrons and protons.

Acknowledgment. V.S.B. acknowledges a generous allocation of supercomputer time from the National Energy Research Scientific Computing (NERSC) center and financial support from Research Corporation, Research Innovation Award # RI0702, a Petroleum Research Fund Award from the American Chemical Society PRF # 37789-G6, a junior faculty award from the F. Warren Hellman Family, the National Science Foundation (NSF) Career Program Award CHE # 0345984, the NSF Nanoscale Exploratory Research (NER) Award ECS # 0404191, the Alfred P. Sloan Fellowship (2005−2006), a Camille Dreyfus Teacher-Scholar Award for 2005, and a Yale Junior Faculty Fellowship in the Natural Sciences (2005−2006). G.W.B acknowledges support from the National Institutes of Health Grant GM32715.

References

(1) Warshel, A.; Levitt, M. *J. Mol. Biol.* **1976**, *103*, 227−249.

(2) Dapprich, S.; Komaromi, I.; Byun, K. S.; Morokuma, K.; Frisch, M. J. *THEOCHEM* **1999**, *461*, 1−21.

(3) Gascón, J. A.; Leung, S. S. F.; Batista, E. R.; Batista, V. S. *J. Chem. Theory Comput.* **2006**, *2*, 175−186.

(4) Ferreira, K. N.; Iverson, T. M.; Maghlaoui, K.; Barber, J.; Iwata, S. *Science* **2004**, *303*, 1831−1838.

(5) Vrettos, J. S.; Limburg, J.; Brudvig, G. W. *Biochim. Biophys. Acta* **2001**, *1503*, 229−245.

(6) Diner, B. A.; Babcock, G. T. In *Oxygenic Photosynthesis*: *The Light Reactions*; Ort, D. R., Yocum, C. F., Eds.; Kluwer Academic Publishers: Dordrecht, The Netherlands, 1996; pp 213−247.

(7) Debus, R. J. *Biochim. Biophys. Acta* **1992**, *1102*, 269−352.

(8) Witt, H. T. *Phys. Chem. Chem. Phys.* **1996**, *100*, 1923−1942.

(9) Britt, R. D. In *Oxygenic Photosynthesis*: *The Light Reactions*; Ort, D. R., Yocum, C. F., Eds.; Kluwer Academic Publishers: Dordrecht, The Netherlands, 1996; pp 137−159.

(10) Barber, J. *Quart. Rev. Biophys.* **2003**, *36*, 71−89.

(11) Yachandra, V. K.; Sauer, K.; Klein, M. P. *Chem. Rev.* **1996**, *96*, 2927−2950.

(12) Lundberg, M.; Siegbahn, P. E. M. *Phys. Chem. Chem. Phys.* **2004**, *6*, 4772−4780.

(13) McEvoy, J. P.; Gascón, J. A.; Sproviero, E. M.; Batista, V. S.; Brudvig, G. W. In *Photosynthesis*: *Fundamental Aspects to Global Perspectives*; Bruce, D., van der Est, A., Eds.; Allen Press Inc.: Lawrence, Kansas, 2005; Vol. 1, pp 278−280.

(14) McEvoy, J. P.; Gascón, J. A.; Batista, V. S.; Brudvig, G. W. *Photochem. Photobiol. Sci.* **2005**, *4*, 940−949.

(15) Joliot, P.; Barbieri, G.; Chabaud, R. *Photochem. Photobiol.* **1969**, *10*, 309−329.

(16) Kok, B.; Forbush, B.; McGloin, M. *Photochem. Photobiol.* **1970**, *11*, 457−475.

(17) Messinger, J.; Badger, M.; Wydrzynski, T. *Proc. Natl. Acad. Sci. U.S.A.* **1995**, *92*, 3209−3213.

(18) Messinger, J. *Phys. Chem. Chem. Phys.* **2004**, *6*, 4764−4771.

(19) McEvoy, J. P.; Brudvig, G. W. *Phys. Chem. Chem. Phys.* **2004**, *6*, 4754−4763.

(20) Robblee, J. H.; Cinco, R. M.; Yachandra, V. K. *Biochim. Biophys. Acta* **2001**, *1503*, 7−23.

(21) Pecoraro, V. L.; Baldwin, M. J.; Caudle, M. T.; Hsieh, W. Y.; Law, N. A. *Pure Appl. Chem.* **1998**, *70*, 925−929.

(22) Barber, J.; Ferreira, K. N.; Maghlaoui, K.; Iwata, S. *Phys. Chem. Chem. Phys.* **2004**, *6*, 4737−4742.

(23) Britt, R. D.; Peloquin, J. M.; Gilchrist, M. L.; Aznar, C. P.; Dicus, M. M.; Robblee, J.; Messinger, J. *Biochim. Biophys. Acta* **2004**, *1655*, 158−171.

(24) Yachandra, V. K.; Klein, K. S. M. P. *Chem. Rev.* **1996**, *96*, 2927−2950.

(25) Hillier, W.; Wydrzynski, T. *Biochemistry* **2000**, *39*, 4399−4405.

(26) Hillier, W.; Wydrzynski, T. *Phys. Chem. Chem. Phys.* **2004**, *6*, 4882−4889.

(27) Mukhopadhyay, S.; Mandal, S. K.; Bhaduri, S.; Armstrong, W. H. *Chem. Rev.* **2004**, *104*, 3981−4026.

(28) Miller, A. F.; Brudvig, G. W. *Biochim. Biophys. Acta* **1991**, *1056*, 1−18.

(29) Britt, R. D.; Peloquin, J. M.; Campbell, K. A. *Annu. Rev. Biophys. Biomol. Struct.* **2000**, *29*, 463−495.

(30) Mino, H.; Kawamori, A. *Biochim. Biophys. Acta* **2001**, *1503*, 112−122.

(31) Boussac, A.; Un, S.; Horner, O.; Rutherford, A. W. *Biochemistry* **1998**, *37*, 4001−4007.

(32) Kulik, L.; Epel, B.; Messinger, J.; Lubitz, W. *Photosynth. Res.* **2005**, *84*, 347−353.

(33) Dau, H.; Liebisch, P.; Haumann, M. *Anal. Bioanal. Chem.* **2003**, *376*, 562−583.

(34) Liang, W. C.; Roelofs, T. A.; Cinco, R. M.; Rompel, A.; Latimer, M. J.; Yu, W. O.; Sauer, K.; Klein, M. P.; Yachandra, V. K. *J. Am. Chem. Soc.* **2000**, *122*, 3399−3412.

(35) Yachandra, V. K. *Philos. Trans. R. Soc. London, Ser. B* **2002**, *357*, 1347−1357.

(36) Dau, H.; Liebisch, P.; Haumann, M. *Phys. Chem. Chem. Phys.* **2004**, *6*, 4781−4792.

(37) Robblee, J. H.; Messinger, J.; Cinco, R. M.; McFarlane, K. L.; Fernandez, C.; Pizarro, S. A.; Sauer, K.; Yachandra, V. K. *J. Am. Chem. Soc.* **2002**, *124*, 7459−7471.

(38) Haumann, M.; Muller, C.; Liebisch, P.; Iuzzolino, L.; Dittmer, J.; Grabolle, M.; Neisius, T.; Meyer-Klaucke, W.; Dau, H. *Biochemistry* **2005**, *4*, 1894−1908.

(39) Ke, B. *Photosynthesis*: *Photobiochemistry and Photobiophysics*; Academic Publishers: Dordrecht, The Netherlands, 2001.

(40) Berthomieu, C.; Hienerwadel, R.; Boussac, A.; Breton, J.; Diner, B. A. *Biochemistry* **1998**, *37*, 10547−10554.

(41) Chu, H.; Hillier, W.; Debus, R. J. *Biochemistry* **2004**, *43*, 3152−3166.

(42) Debus, R. J.; Strickler, M. A.; Walker, L. M.; Hillier, W. *Biochemistry* **2005**, *44*, 1367−1374.

(43) Strickler, M. A.; Walker, L. M.; Hillier, W.; Debus, R. J. *Biochemistry* **2005**, *44*, 8571−8577.

(44) Kimura, Y.; Mizusawa, N.; Yamanari, T.; Ishii, A.; Ono, T. *J. Biol. Chem.* **2005**, *280*, 2078−2083.

(45) Roffey, R. A.; Kramer, D. M.; Govindjee; Sayre, R. T. *Biochim. Biophys. Acta* **1994**, *1185*, 257−270.

(46) Kramer, D. M.; Roffey, R. A.; Govindjee; Sayre, R. T. *Biochim. Biophys. Acta* **1994**, *1185*, 228−237.

(47) Debus, R. J. *Biochim. Biophys. Acta* **2001**, *1503*, 164−186.

(48) Diner, B. A. *Biochim. Biophys. Acta* **2001**, *1503*, 147−163.

(49) Zouni, A.; Witt, H. T.; Kern, J.; Fromme, P.; Krauss, N.; Saenger, W.; Orth, P. *Nature* **2001**, *409*, 739−743.

(50) Kamiya, N.; Shen, J. R. *Proc. Natl. Acad. Sci. U.S.A.* **2003**, *100*, 98−103.

(51) Biesiadka, J.; Loll, B.; Kern, J.; Irrgang, K. D.; Zouni, A. *Phys. Chem. Chem. Phys.* **2004**, *6*, 4733−4736.

(52) Loll, B.; Kern, J.; Saenger, W.; Zouni, A.; Biesiadka, J. *Nature* **2005**, *438*, 1040−1044.

(53) Yano, J.; Kern, J.; Irrgang, K.; Latimer, M. J.; Bergmann, U.; Glatzel, P.; Pushkar, Y.; Biesiadka, J.; Loll, B.; Sauer, K.; Messinger, J.; Zouni, A.; Yachandra, V. K. *Proc. Natl. Acad. Sci. U.S.A.* **2005**, *102*, 12047−12052.

(54) Sauer, K.; Yachandra, V. K. *Biochim. Biophys. Acta* **2004**, *1655*, 140−148.

(55) Dau, H.; Iuzzolino, L.; Dittmer, J. *Biochim. Biophys. Acta* **2001**, *1503*, 24−39.

(56) Crespo, A.; Scherlis, D.; Martí, M. A.; Ordejon, P.; Roitberg, A. E.; Estrin, D. A. *J. Phys. Chem. B* **2003**, *107*, 13728−13736.

(57) Martí, M. A.; Crespo, A.; Bari, S. E.; Doctorovich, F. A.; Estrin, D. A. *J. Phys. Chem. B* **2004**, *108*, 18073−18080.

(58) Fernández, M. L.; Martí, M. A.; Crespo, A.; Estrin, D. A. *J. Biol. Inorg. Chem.* **2005**, *10*, 595−604.

(59) Crespo, A.; Martí, M. A.; Estrin, D. A.; Roitberg, A. E. *J. Am. Chem. Soc.* **2005**, *127*, 6940−6941.

(60) Friesner, R.; Guallar, V. *Annu. Rev. Phys. Chem.* **2005**, *56*, 389−427.

(61) Guallar, V.; Jacobson, M.; McDermott, A.; Friesner, R. A. *J. Mol. Biol.* **2004**, *337*, 227−239.

(62) Friesner, R. A.; Baik, M.; Gherman, B. F.; Guallar, V.; Wirstam, M.; Murphy, R. B.; Lippard, S. J. *Coord. Chem. Rev.* **2003**, *238*−*239*, 267−290.

(63) Gherman, B.; Goldberg, S.; Cornish, V. W.; Friesner, R. *J. Am. Chem. Soc.* **2004**, *126*, 7652−7664.

(64) Derat, E.; Cohen, S.; Shaik, S.; Altun, A.; Thiel, W. *J. Am. Chem. Soc.* **2005**, *127*, 13611−13621.

(65) Lin, H.; Schoneboom, J.; Cohen, S.; Shaik, S.; Thiel, W. *J. Phys. Chem. B* **2004**, *108*, 10083−10088.

(66) Schoneboom, J.; Cohen, S.; Lin, H.; Shaik, S.; Thiel, W. *J. Am. Chem. Soc.* **2004**, *126*, 4017−4034.

(67) Lundberg, M.; Blomberg, M.; Siegbahn, P. *Top. Curr. Chem.* **2004**, *238*, 79−112.

(68) Siegbahn, P. E. M. *J. Biol. Inorg. Chem.* **2003**, *8*, 567−576.

(69) Gascón, J. A.; Batista, V. S. *Biophys. J.* **2004**, *87*, 2931−2941.

(70) Gascón, J. A.; Sproviero, E. M.; Batista, V. S. *J. Chem. Theory Comput.* **2005**, *1*, 674−685.

(71) Gascón, J. A.; Sproviero, E. M.; Batista, V. S. *Acc. Chem. Res.* **2006**, *39*, 184−193.

(72) Hendry, G.; Wydrzynski, T. *Biochemistry* **2003**, *42*, 6209−6217.

(73) Frisch, M. J.; Trucks, G. W.; Schlegel, H. B.; Scuseria, G. E.; Robb, M. A.; Cheeseman, J. R.; Montgomery, J. A., Jr.; Vreven, T.; Kudin, K. N.; Burant, J. C.; Millam, J. M.; Iyengar, S. S.; Tomasi, J.; Barone, V.; Mennucci, B.; Cossi, M.; Scalmani, G.; Rega, N.; Petersson, G. A.; Nakatsuji, H.; Hada, M.; Ehara, M.; Toyota, K.; Fukuda, R.; Hasegawa, J.; Ishida, M.; Nakajima, T.; Honda, Y.; Kitao, O.; Nakai, H.; Klene, M.; Li, X.; Knox, J. E.; Hratchian, H. P.; Cross, J. B.; Adamo, C.; Jaramillo, J.; Gomperts, R.; Stratmann, R. E.; Yazyev, O.; Austin, A. J.; Cammi, R.; Pomelli, C.; Ochterski, J. W.; Ayala, P. Y.; Morokuma, K.; Voth, G. A.; Salvador, P.; Dannenberg, J. J.; Zakrzewski, V. G.; Dapprich, S.; Daniels, A. D.; Strain, M. C.; Farkas, O.; Malick, D. K.;

Rabuck, A. D.; Raghavachari, K.; Foresman, J. B.; Ortiz, J. V.; Cui, Q.; Baboul, A. G.; Clifford, S.; Cioslowski, J.; Stefanov, B. B.; Liu, G.; Liashenko, A.; Piskorz, P.; Komaromi, I.; Martin, R. L.; Fox, D. J.; Keith, T.; Al-Laham, M. A.; Peng, C. Y.; Nanayakkara, A.; Challacombe, M.; Gill, P. M. W.; Johnson, B.; Chen, W.; Wong, M. W.; Gonzalez, C.; Pople, J. A. *Gaussian 03*, revision A.1; Gaussian, Inc.: Wallingford, CT, 2003.

(74) Vacek, G.; Perry, J. K.; Langlois, J. M. *Chem. Phys. Lett.* **1999**, *310*, 189−194.

(75) Jaguar 5.5; Schroedinger, LLC: Portland, OR, 2003.

(76) Note that all amino acid residues are labeled according to the one-letter standard nomenclature and correspond to the D1 protein subunit unless otherwise indicated.

(77) Sproviero, E. M.; Gascón, J. A.; McEvoy, J. P.; Brudvig, G. W.; Batista, V. S. *J. Inorg. Biochem.* **2005**, *100*, 786−800.

(78) Noodleman, L. *J. Chem. Phys.* **1981**, *74*, 5737−5743.

(79) Noodleman, L.; Davidson, E. R. *Chem. Phys.* **1986**, *109*, 131−143.

(80) Noodleman, L.; Case, D. A. *Adv. Inor. Chem.* **1992**, *38*, 423−470.

(81) Noodleman, L.; Peng, C. Y.; Case, D. A.; Mouesca, J. M. *Coord. Chem. Rev.* **1995**, *144*, 199−244.

(82) Kronig, R. *Z. Phys.* **1931**, *70*, 317−323.

(83) Kronig, R. *Z. Phys.* **1932**, *75*, 190−210.

(84) Sayers, D. E.; Stern, E. A.; Lytle, F. W. *Phys. Rev. Lett.* **1971**, *27*, 1204−1207.

(85) Stern, E. *Phys. Rev. B* **1974**, *10*, 3027−3027.

(86) Pendry, J. In *Low Energy Electron Diffraction*; Academic Press: New York, 1974; pp 20−35.

(87) Lee, P.; Pendry, J. *Phys. Rev. B* **1975**, *11*, 2795−2811.

(88) Ashley, C.; Doniach, S. *Phys. Rev. B* **1975**, *11*, 1279−1288.

(89) Gonis, A. *Green Functions for Ordered and Disordered Systems*; Elsevier: Amsterdam, 1992.

(90) Ankudinov, A. L.; Ravel, B.; Rehr, J. J.; Conradson, S. D. *Phys. Rev. B* **1998**, *58*, 7565−7576.

(91) Ankudinov, A. L.; Bouldin, C.; Rehr, J. J.; Sims, J.; Hung, H. *Phys. Rev. B* **2002**, *65*, 104107−104118.

(92) The capabilities of the DFT B3LYP functional for predicting Mn−Mn distances in biomimetic oxomanganese complexes have been recently investigated.[77]

(93) Pospisil, P.; Haumann, M.; Dittmer, J.; Sole, V. A.; Dau, H. *Biophys. J.* **2003**, *84*, 1370−1386.

(94) Yachandra, V. K.; DeRose, V. J.; Latimer, M. J.; Mukerji, L.; Sauer, K.; Klein, M. P. *Science* **1993**, *260*, 675−679.

(95) Ono, T. A.; Noguchi, T.; Inoue, Y.; Kusunoki, M.; Matsushita, T.; Oyanagi, H. *Science* **1992**, *258*, 1335−1337.

(96) Roelofs, T. A.; Liang, W. C.; Latimer, M. J.; Cinco, R. M.; Rompel, A.; Andrews, J. C.; Sauer, K.; Yachandra, V. K.; Klein, M. P. *Proc. Natl. Acad. Sci. U.S.A.* **1996**, *93*, 3335−3340.

(97) Bergmann, U.; Grush, M. M.; Horne, C. R.; DeMarois, P.; Penner-Hahn, J. E.; Yocum, C. F.; Wright, D. W.; Dube, C. E.; Armstrong, W. H.; Christou, G.; Eppley, H. J.; Cramer, S. P. *J. Phys. Chem. B* **1998**, *102*, 8350−8352.

(98) Iuzzolino, L.; Dittmer, J.; Dau, H. *Biochemistry* **1998**, *37*, 17112−17119.

(99) Messinger, J.; Robblee, J. H.; Bergmann, U.; Fernandez, C.; Glatzel, P.; Visser, H.; Cinco, R. M.; McFarlane, K. L.; Bellacchio, E.; Pizarro, S. A.; Cramer, S. P.; Sauer, K.; Klein, M. P.; Yachandra, V. K. *J. Am. Chem. Soc.* **2001**, *123*, 7804−7820.

(100) Zheng, M.; Dismukes, G. C. *Inorg. Chem.* **1996**, *35*, 3307−3319.

(101) Kuzek, D.; Pace, R. J. *Biochim. Biophys. Acta* **2001**, *1503*, 123−137.

(102) Dasgupta, J.; van Willigen, R. T.; Dismukes, G. C. *Phys. Chem. Chem. Phys.* **2004**, *6*, 4793−4802.

(103) Clausen, J.; Beckman, K.; Junge, W.; Messinger, J. *Plant Physiol.* **2005**, *139*, 1444−1450.

(104) Kühne, H.; Szalai, V. A.; Brudvig, G. W. *Biochemistry* **1999**, *38*, 6604−6613.

(105) Wincencjusz, H.; van Gorkom, H. J.; Yocum, C. F. *Biochemistry* **1997**, *36*, 3663−3670.

(106) Olesen, K.; Andreasson, L. E. *Biochemistry* **2003**, *42*, 2025−2035.

(107) Force, D. A.; Randall, D. W.; Britt, R. D. *Biochemistry* **1997**, *36*, 12062−12070.

(108) Clemens, K. L.; Force, D. A.; Britt, R. D. *J. Am. Chem. Soc.* **2002**, *124*, 10921−10933.

(109) Debus, R. J.; Barry, B. A.; Sithole, I.; Babcock, G. T.; McIntosh, L. *Biochemistry* **1988**, *27*, 9071−9074.

(110) Metz, J. G.; Nixon, P. J.; Rogner, M.; Brudvig, G. W.; Diner, B. A. *Biochemistry* **1989**, *28*, 6960−6969.

(111) Hays, A. M. A.; Vassiliev, I. R.; Golbeck, J. H.; Debus, R. J. *Biochemistry* **1998**, *37*, 11352−11365.

(112) Hays, A. M. A.; Vassiliev, I. R.; Golbeck, J. H.; Debus, R. J. *Biochemistry* **1998**, *38*, 11851−11865.

(113) Hoganson, C. W.; Babcock, G. T. *Science* **1997**, *277*, 1953−1956.

(114) Ishikita, H.; Saenger, W.; Loll, B.; Biesiadka, J.; Knapp, E. W. *Biochemistry* **2006**, *45*, 2063−2071.

(115) Schlodder, E.; Witt, H. T. *J. Biol. Chem.* **1999**, *274*, 30877−30392.

(116) Junge, W.; Haumann, M.; Ahbrink, R.; Mulkidjanian, A.; Clausen, J. *Philos. Trans. R. Soc. London, Ser. B.* **2002**, *357*, 1407−1418.

(117) Rappaport, F.; Lavergne, J. *Biochim. Biophys. Acta* **2001**, *1503*, 246−259.

(118) Mukerji, I.; Andrews, J. C.; DeRose, V. J.; Latimer, M.; Yachandra, V. K.; Sauer, K.; Klein, M. P. *Biochemistry* **1994**, *33*, 9712−9721.

(119) Ghosh, A.; Taylor, P. R. *Curr. Opin. Chem. Biol.* **2003**, *7*, 113−124.

(120) Ghosh, A.; Taylor, P. R. *J. Chem. Theory Comput.* **2005**, *1*, 597−600.

(121) Ghosh, A.; Steene, E. *J. Biol. Inorg. Chem.* **2001**, *6*, 739−752.

(122) Weiss, R.; Bulach, V.; Gold, A.; Terner, J.; Trautwein, A. X. *J. Biol. Inorg. Chem.* **2001**, *6*, 831−845.

(123) Reiher, M.; Salomon, O.; Hess, B. A. *Theor. Chem. Acc.* **2001**, *107*, 48−55.

(124) Salomon, O.; Reiher, M.; Hess, B. A. *J. Chem. Phys.* **2002**, *117*, 4729−4737.

(125) Holthausen, M. C. *J. Comput. Chem.* **2005**, *26*, 1505−1518.

CT060018L